International Journal of Plasticity 181 (2024) 104079

Contents lists available at ScienceDirect

International Journal of Plasticity

journal homepage: www.elsevier.com/locate/ijplas

Achieving excellent uniform tensile ductility and strength in dislocation-cell-structured high-entropy alloys

Rui Huang[a,b], Lingkun Zhang[a,b], Abdukadir Amar[a,b], Peter K. Liaw[c,*], Tongmin Wang[a,b], Tingju Li[a,b], Yiping Lu[a,b,*]

[a] *Key Laboratory of Solidification Control and Digital Preparation Technology (Liaoning Province), School of Materials Science and Engineering, Dalian University of Technology, Dalian, 116024, China*

[b] *Engineering Research Center of High Entropy Alloy Materials (Liaoning Province), School of Materials Science and Engineering, Dalian University of Technology, Dalian, 116024, China*

[c] *Department of Materials Science and Engineering, The University of Tennessee, Knoxville, TN, 37996, United States*

ARTICLE INFO

Keywords:
High-entropy alloys
Heterogeneous structure
Uniform tensile ductility
Dislocation cell
Mechanical properties

ABSTRACT

Body-centered-cubic (BCC) high-entropy alloys (HEAs) encounter significant challenges in obtaining a high uniform tensile ductility (UTD). A dense dislocation-cell (DC) structure is produced in a heterogeneously grained HEA under tensile deformation, resulting from the anchored dislocation motion by grain interior elemental segregation. This fluctuation in elemental concentration is facilitated by thermomechanical processing. The activation of multiple-slip mechanisms, prompted by strain incompatibility among grains of varying sizes, significantly propels this process forward. This novel DC structure simultaneously increased the UTD (by 349.1 %) and yield strength ($\sigma_{0.2}$, by 29.0 %) for a stable BCC HEA. Specifically, the single-phase alloy achieved a record-high UTD of 7.5 % and an $\sigma_{0.2}$ of $>$ 1,200 MPa, outperforming the counterparts of all the single-phase BCC HEAs. We employed a combination of transmission electron microscopy, in-situ scanning electron microscopy tensile testing coupled with an electron backscatter diffraction technology to investigate underlying strengthening mechanisms and identified that the serious stress concentration as a result of prevalent planar slip caused premature failure and localized strain of common BCC HEAs. At the initial stage of deformation, the DC structure promoted the activation of multiple slip systems and facilitated the extension of a plastic flow across the sample volume, effectively weakening stress concentration and premature failure. The extended plasticity zone and intensified dislocation interactions contributed to the increased UTD and $\sigma_{0.2}$. These findings offer valuable inspiration for tailoring alloy properties via microstructure strategies and promoting their adoption in advanced manufacturing.

Abbreviations: SF, Stack faults; DC, Dislocation-cell; XRD, X-ray diffraction; HEAs, High-entropy alloys; STEM-BF, STEM bright-field; WHR, Work hardening rate; BCC, Body-centered-cubic; FCC, Face-centered-cubic; IPF, Inverse-pole figures; WHA, Work hardening ability; UTD, Uniform tensile ductility; HDI, Hetero-deformation induced; KAM, Kernel Average Misorientation; TWIP, Twinning induced plasticity; SEM, Scanning electron microscope; HDDWs, High-density dislocation walls; SAED, Selected area electron diffraction; EBSD, Electron backscatter diffraction; AC, As-cast; HG, Sample with heterogeneous grain size; UG, Sample with uniform grain size; GNDs, Geometrically necessary dislocations; SMDIC, Strain measurement by the digital image correction; HAADF-STEM, High-angle annular dark-field-scanning transmission electron microscopy.

* Corresponding authors.
E-mail addresses: pliaw@utk.edu (P.K. Liaw), luyiping@dlut.edu.cn (Y. Lu).

https://doi.org/10.1016/j.ijplas.2024.104079
Received 12 May 2024; Received in revised form 9 July 2024;
Available online 31 July 2024

1. Introduction

Body-centered-cubic (BCC) high-entropy alloys (HEAs), predominantly composed of high melting-temperature elements, have garnered significant attention due to their exceptional mechanical properties within a wide temperature range, holding promise as the next-generation structural materials (Cantor et al., 2004; Lei et al., 2018; Senkov et al., 2011b; Tan et al., 2024; Yeh et al., 2004). However, despite their inherent high strength, BCC HEAs often exhibit limited work-hardening ability (WHA) and uniform tensile ductility (UTD) during tensile deformation (Sheikh et al., 2016; Wang et al., 2024; Yurchenko et al., 2023b; Zhang et al., 2023b). While some alloys exhibited high yield strength ($\sigma_{0.2}$), their poor WHA restricts widespread industrial uses as structural materials, particularly in applications like aircraft-engine-compressor discs and rotor blades, where the inability to withstand accidental overloads poses significant threats to both equipment safety and personal well-being. Also, poor UTD severely damages the forming and machining capabilities of these alloys, thus limiting their practical applications.

The constrained UTD in a stable single-phase BCC HEA primarily arises from the prompt onset of the localized deformation and necking following yielding, attributed to the less activation of the slip system during deformation and insufficient dislocation interactions, which reduced dislocation-motion resistance (Wang et al., 2023a). In contrast to face-centered-cubic (FCC) HEAs or twinning-induced plasticity (TWIP) steel, where stack faults (SF) and deformation twins often interact intensely with dislocations, facilitating high UTD. Such interactions are rarely observed in deformed BCC HEAs due to their elevated SF energy at room temperature (Cheng et al., 2018; Ding et al., 2018; Gupta et al., 2022; Kaushik et al., 2021; Kishore et al., 2023; Madivala et al., 2019, 2018; Naeem et al., 2020; Pan et al., 2021; Wei et al., 2022; Wu and Shao, 2023). Up to now, only a few methods have been proposed to enhance the UTD of BCC-structured HEAs. Prior attempts to enhance mechanical properties via structural design, utilizing cold rolling and full recrystallization to achieve finer grain sizes and uniform microstructures, have yielded negligible improvements in UTD as these methods have not changed the fundamental plastic-deformation features of BCC alloys (Yurchenko et al., 2023a; Zhang et al., 2023a). Additionally, the strength increment achieved through this method is limited due to inadequate activation of dislocations required for coordinated deformation, thereby insufficiently enhancing alloy strength (Li et al., 2023). The transformation-induced plasticity concept could improve the alloy UTD while a sustained heavy loss of $\sigma_{0.2}$ accompanies it (Wen et al., 2021).

Spatially heterogeneous-structure strengthening, incorporating non-uniform grain sizes or chemical compositions, has been employed to augment alloy UTD and/or strength (Dasari et al., 2023; Fu et al., 2022; Fujita et al., 2018; Hasan et al., 2019; Kishore et al., 2023; Kumar et al., 2023; Peng et al., 2021). In BCC HEAs, inducing heterogeneous structures often involves forming second phases or simple complexes. However, the addition of small atomic-radius elements to some BCC-structured HEAs, allowing the accommodation of additional interstitial atoms in the crystal lattice, is unsuitable for alloy systems primarily composed of elements with small atomic radii (Ma and Wu, 2019). While engineering heterogeneous structures in ductile alloys, such as FCC HEAs, through high-pressure torsion, cold-rolling, and heat treatment, has shown success in improving $\sigma_{0.2}$ (Bahramyan et al., 2020; Cheng et al., 2018; Jeong and Kim, 2021; Pan et al., 2021), the substantial increase in dislocations, despite enhancing strength, leads to severe stress concentration when fundamental plastic deformation features and dislocation-motion modes remain unchanged, thereby potentially deteriorating alloy ductility (Chu et al., 2024; Karthik et al., 2022; Liu et al., 2022). Significantly, limited focus has been directed towards the heterostructure design through severe deformation in single-phase BCC HEAs due to the intrinsic brittleness of most reported alloys in the literature. Consequently, it appears unfeasible to enhance the UTD of BCC HEAs in this way.

In this study, a heterogeneous grain-size microstructure is intentionally designed and prepared in a single-phase BCC-structured $Ti_{37}Nb_{27}Zr_{23}Al_7V_6$ (atomic percent, at.%) HEA. We also studied alloys with a coarse-grain microstructure, and uniform fine-grain microstructure for comparison. At the initial stage of tensile testing, the heterogeneous-microstructure resulted in the unexpected formation of a dense dislocation-cell (DC) structure, a novel occurrence in BCC HEAs, as opposed to the anticipated high-density dislocation walls (HDDWs) induced by conventional localized deformation. The DC structure increased the resistance to dislocation motion and obstructed their slip path. This trend promoted the activation of multiple-slip systems and facilitated the extension of the plastic flow across the sample volume, effectively delaying localized deformation and stress concentration, thereby mitigating a premature formation of microcracks and associated specimen failure. Moreover, the extend uniform deformation, together with amplified dislocation interactions, contributes to a marked improvement in UTD and $\sigma_{0.2}$ of the alloy. These findings help discover the essential origin of the poor UTD for BCC HEAs and offer valuable inspiration for tailoring mechanical properties, which is essential to improve usage safety factors and promote their industrial applications in advanced manufacturing.

2. Materials and methods

2.1. Materials preparation

The equilibrium phase diagram of the $Ti_{37}Nb_{27}Zr_{23}Al_7V_6$ HEA was obtained, using the commercial software of Pandat and Pan-RHEAs thermodynamic database (CompuTherm. LLC). The HEA was synthesized via vacuum arc melting, employing a mixture of pure metals with a purity $\geq$ 99.9 wt percent (wt.%). The furnace chamber underwent evacuation to a pressure lower than 3.0×10^{-3} Pa, subsequently filled with high-purity argon gas to prevent oxidation. To eliminate residual oxygen, a Ti ingot was initially melted before alloy melting. The resulting ingots underwent multiple re-melting and flipping cycles, ensuring chemical homogeneity. Magnetic stirring was employed during melting to ensure uniformity. Some ingots underwent cold rolling with a 75 % reduction in thickness. Subsequently, certain cold-rolled plates were subjected to the heat treatment at 680 °C [0.38 of melting temperature (T_m), Supplementary Fig. 1] for 30 min, followed by 600 °C for an additional 30 min. Others underwent the heat treatment at 900 °C (higher than 0.5 T_m, Supplementary Fig. 1) for 30 min, followed by 600 °C for 30 min. Each heat-treatment cycle was succeeded by water

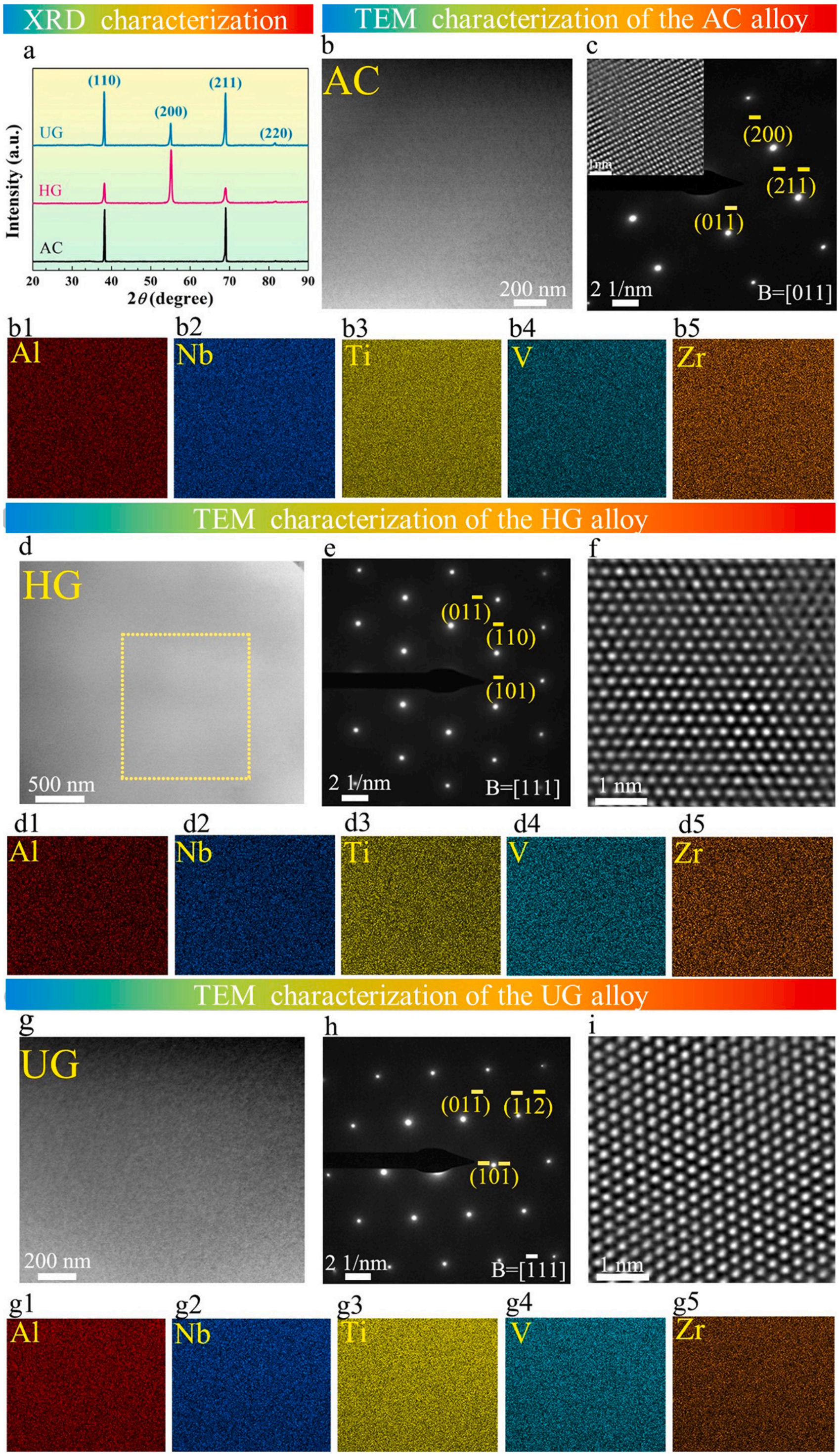

Fig. 1. Microstructural characterization of the three specimens. (a) XRD patterns of the AC, HG, and UG samples. (b) HAADF-STEM image and (c) corresponding SAED patterns of the AC specimen. The inset in c is the close-up HAADF-STEM image that shows an atomic arrangement of the AC alloy. (b1 - b5) Elemental-distribution maps correspond to the image (b). (d) HAADF-STEM image and (e) corresponding SAED patterns of the HG specimen. (f) Close-up HAADF-STEM image that presents an atomic arrangement of the HG alloy. (d1 - d5) Elemental-distribution maps correspond to the yellow square in image (d). (g) HAADF-STEM image and (h) corresponding SAED patterns of the UG specimen. (i) Close-up HAADF-STEM image that shows an atomic arrangement of the UG alloy. (g1 - g5) Elemental-distribution maps correspond to the image (g).

quenching. The Fe foils were used to encase the cold-rolled plates during annealing to prevent potential oxidation at high temperatures. The as-cast specimen was denoted as the AC sample. The specimens subjected to heat treatments at 680 °C and 900 °C were identified as the HG and UG specimens, respectively. For tensile testing at room temperature, sheet specimens with a gauge length of 10 mm and a cross-section of 2 × 1.8 mm were fabricated, using a wire-cutting machine, and mechanically polished with 2000 grits SiC paper.

2.2. Mechanical-properties characterization

Quasi-static tensile tests and loading-unloading-reloading (LUR) tests were performed at room temperature, employing a strain rate of 1.0×10^{-3}/s, using an electronic universal testing machine (Suns-UTM4000). Three samples were tested for each condition to ensure repeatability. For these tests, a high-precision non-contact video extensometer (NCM-2D) facilitated accurate measurements of displacements at room and high temperatures. In LUR tests, once reaching to a designated strain, the samples were unloaded in stress-control mode to 50 MPa at unloading rate of 20 MP/s, followed by reloading at a strain rate of 1.0×10^{-3}/s to the same applied stress before the next unloading. Hardness distributions of the samples were evaluated both before and after tensile tests using a Vickers indenter under a load of 500 g, maintaining a dwell time of 15 s. An average hardness value for each position was derived from three indentations, and the resulting error bar was plotted accordingly. Hardness testing was performed on three samples for each condition to avoid accidental error. Furthermore, the overall specimen’s average hardness was determined from 30 indentations, with the error bar represented in the plot.

In-situ scanning electron microscope (SEM) tensile tests for the AC, HG, and UG alloys were conducted on a field emission SEM (IT800 SHL) equipped with an electron backscatter diffraction (EBSD, symmetry 2) detector. The specimens with gauge dimensions of 2 × 1.2 × 1 mm were prepared using a wire-cutting machine. Each specimen was ground with 2000 SiC paper, and then polished by SiO_2 suspension until a mirror finish. The mirror specimens were electrochemically polished in a mixture of 10 vol percent (vol.%) perchloric and 90% anhydrous ethanol at 263 K. The in-situ tensile testing was conducted at a strain rate of 1.0×10^{-3}/s under a displacement control mode. The SEM and EBSD characterization were employed to record the evolution of the microstructure at different strains.

2.3. Microstructure characterization

The microstructure analysis involved the use of an X-ray diffraction (XRD, Bruker) and a SEM equipped with EBSD, alongside a transmission electron microscope (TEM, FEI Talos F200X). To prepare TEM specimens, initial mechanical grinding reduced the thickness to 30 μm, followed by further thinning to electron transparency via ion milling employing an ion thinning system (Gatan 695). The detailed ion milling process is described as follows. The specimen was thinned by Ga ion at a voltage of 5 Kev and an ion gun angle of ± 8 ° until a micro-pore appeared at the center of the sample. Then, we need to trim the edges of the micro-pore in multiple steps by progressively reducing the voltage and gun angle of the Ga ion. The initial ion-milling voltage was 4.5 Kev, and an ion-gun angle was ± 6 °, decreasing the voltage to 4 Kev and ion-gun angle of ± 4 ° after 5 min. The working voltage further reduced to 3 Kev coupled with the ion-gun angle contraction to ± 3 ° after working 5 min under the voltage of 4 Kev.

3. Results

3.1. Microstructural characterization before tensile testing

The designed alloy demonstrated remarkable structural stability. Fig. 1a illustrates the XRD patterns of the AC and the other two alloys, highlighting that despite undergoing cold rolling and recrystallization annealing, the single-phase BCC structure of the samples

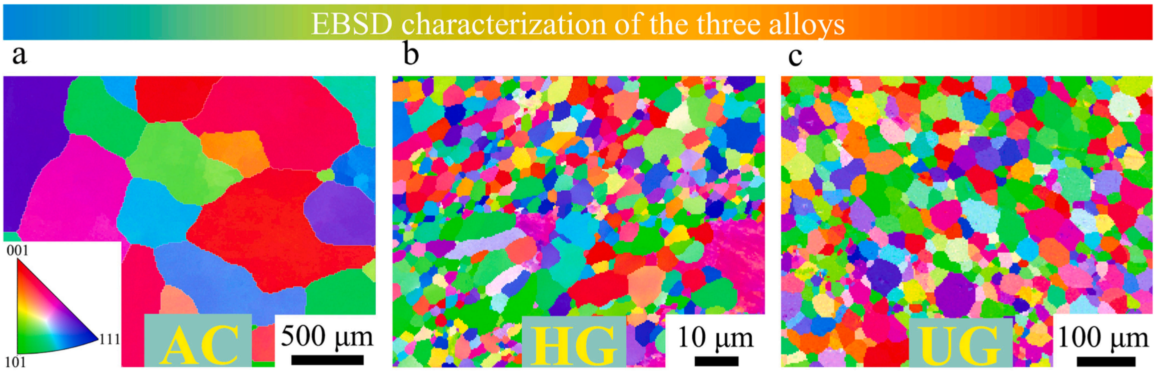

Fig. 2. Microstructural characterization of the three specimens. EBSD-IPF maps of the (a) AC specimen, (b) HG specimen, and (c) UG specimen. Colors in the IPF maps correspond to crystallographic orientations according to the key stereographic triangle shown in the inset of image (a).

remained unchanged. We also confirmed this result by high-angle annular dark-field-scanning transmission electron microscopy (HAADF-STEM) images and selected area electron diffraction (SAED) patterns [Figs. 1(b, c, d, e, g, and h)]. Furthermore, we did not detect any obvious elemental segregation in the three samples [Figs. 1(b1 - b5, d1 - d5, and g1 - g5)].

Figs. 2(a – c) display the EBSD inverse-pole figures (IPF) maps and grain-size distribution maps of the AC, HG, and UG alloys [Supplementary Figs. 2(a - c)], revealing significant differences in the grain size and microstructure homogeneity. In the AC alloy [Fig. 2a and Supplementary Fig. 2a], coarse grains (CGs) averaging approximately 421 μm in size are observed, consistent with a typical grain morphology found in most as-cast HEAs (An et al., 2021). However, the HG and UG specimens exhibit notably finer grain structures, presenting a sharp contrast to the AC specimen. The HG specimen comprises grains with an average size of 3.16 μm [Fig. 2b and Supplementary Fig. 2b], and that of the UG alloy is 24.43 μm [Fig. 2c and Supplementary Fig. 2c]. Note that a substantial variation in the grain size exists within the HG alloy. Specifically, the grain-size difference between the largest and smallest grains is 13 times in the HG sample, whereas in the UG sample, this difference is 7 times. Furthermore, we normalized the grain size, (d), by the average grain size, ($\bar{d}$), for each of the three alloys as the d in the HG samples differs by two orders of magnitude from that in the AC sample. A wide tail phenomenon was observed in the HG sample (Supplementary Fig. 2e) compared to those on the other two samples [Supplementary Figs. 2(d, f)]. Furthermore, the standard deviations of the normalized grain size are 0.58, 0.64, and 0.54 for AC, HG, and UG samples, respectively. Although the relative frequency of CGs with d greater than 20 μm is very low (Supplementary Fig. 2b), they account for a high areal fraction within the HG sample (Supplementary Fig. 2 h). All the above demonstrate that the AC and UG samples have a more uniform microstructure than the HG sample.

3.2. Mechanical properties

In Fig. 3a, the tensile engineering stress-strain curves of the alloys tested at room temperature are presented. Remarkably, the $\sigma_{0.2}$ of the HG alloy surpasses 1200 MPa, notably higher than the 930 MPa for the AC alloy and 1070 MPa for the UG alloy. This elevated $\sigma_{0.2}$ in the HG alloy stands out, exceeding almost all reported values of ductile BCC HEAs and even certain conventional commercial Ti and

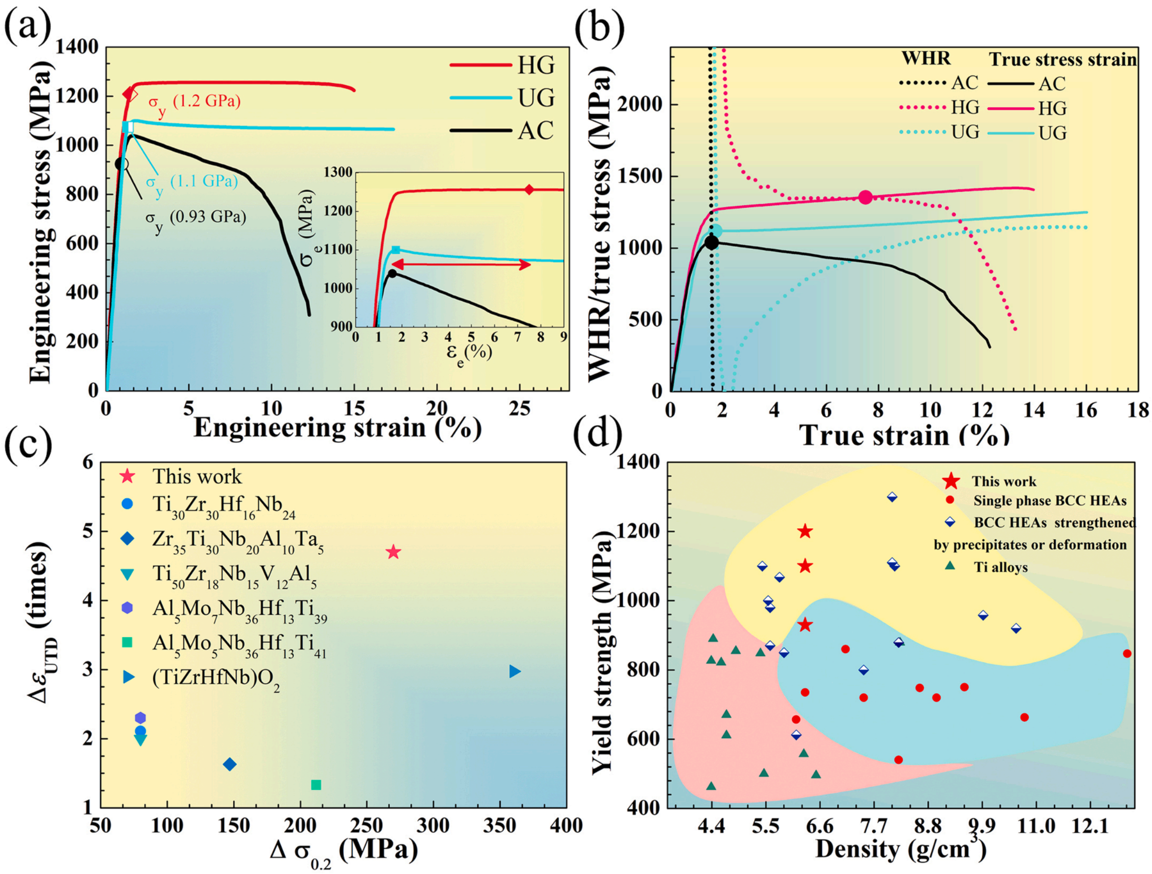

Fig. 3. Mechanical properties of the three alloys. (a) Tensile engineering stress-strain curves of AC, HG, and UG samples. (b) Working hardening rate versus true strain curves and true stress-strain curves of AC, HG, and UG samples. (c) Changes in $\sigma_{0.2}$ and UTD for the HG alloy relative to several classically processed BCC-structured HEAs. (d) Comparison of the three alloys with reported representative BCC HEAs in terms of $\sigma_{0.2}$ and density.

Nb alloys (Fig. 3d) (An et al., 2021; George et al., 2019; Gou et al., 2023; Granberg et al., 2016; Kong et al., 2022; Lei et al., 2018; Li et al., 2022a; Lilensten et al., 2017; Ren et al., 2018; Wang et al., 2019; Wen et al., 2021; Xu et al., 2022; Yan and Zhang, 2020; Zeng et al., 2022; Zhang et al., 2023b, 2021). Generally, the increase in $\sigma_{0.2}$ in a rolled single-phase BCC HEA primarily arises from the refined grain size, contributing only to a limited additional strength within the range of approximately 70 - 150 MPa to the alloy, as observed in the UG alloy. This limitation stems from the dominance of the localized deformation mode during the deformation process at the microscopic scale (Wang et al., 2023a). Notably, the HG alloy demonstrates an outstanding strengthening effect exceeding 250 MPa (Fig. 3c).

Surprisingly, the HG alloy displays simultaneous improvements in both $\sigma_{0.2}$ and ductility post cold rolling and heat treatment, avoiding the longstanding strength-ductility paradox observed in conventional metallic materials and most HEAs (Fig. 3a). The tensile strain to failure increased from 12.3 % for the AC alloy to 15.0 % for the HG alloy and further to 17.4 % for the UG alloy. What is more, note that the improvement in UTD for the HG alloy far exceeds the improvements achieved by all previously reported methods. The enhanced UTD reaches 7.5 % for the HG alloy (inset in Fig. 3a), 4.6 times that of the AC alloy (Fig. 3c), signifying improved machinability ability and a better safety factor.

Additionally, Fig. 3b shows the work-hardening rate (WHR) versus true strain curves and true stress-strain curves of the three samples. The strain that corresponds to the intersection of the WHR curve and true stress is the maximum strain for stability plasticity deformation. The superior WHR of the HG sample to those of the other two samples is apparently significant for elevating UTD effectively. The HG alloy demonstrates superior work-hardening ability, markedly surpassing the AC and UG alloys. The strain measurement by the digital image correlation (SMDIC) was employed to map the full-field strain distribution during tensile deformation (Li et al., 2023). The HG sample exhibits a broader deformation area and less pronounced necking compared to the AC and UG samples, indicating a more uniform and homogenous deformation pattern (Supplementary Fig. 3). Clear necking is observed on the 8 %-strained AC alloy, leading to instability and a subsequent drop in tensile strength. Conversely, the HG alloy shows no discernible necking under the same strain (Supplementary Fig. 4).

An essential inquiry arising from the mechanical-property analysis pertains to why the HG alloy not only improved $\sigma_{0.2}$ but also enhanced UTD and work-hardening capacity without compromising ductility. To elucidate this feature, Vickers-hardness testing was

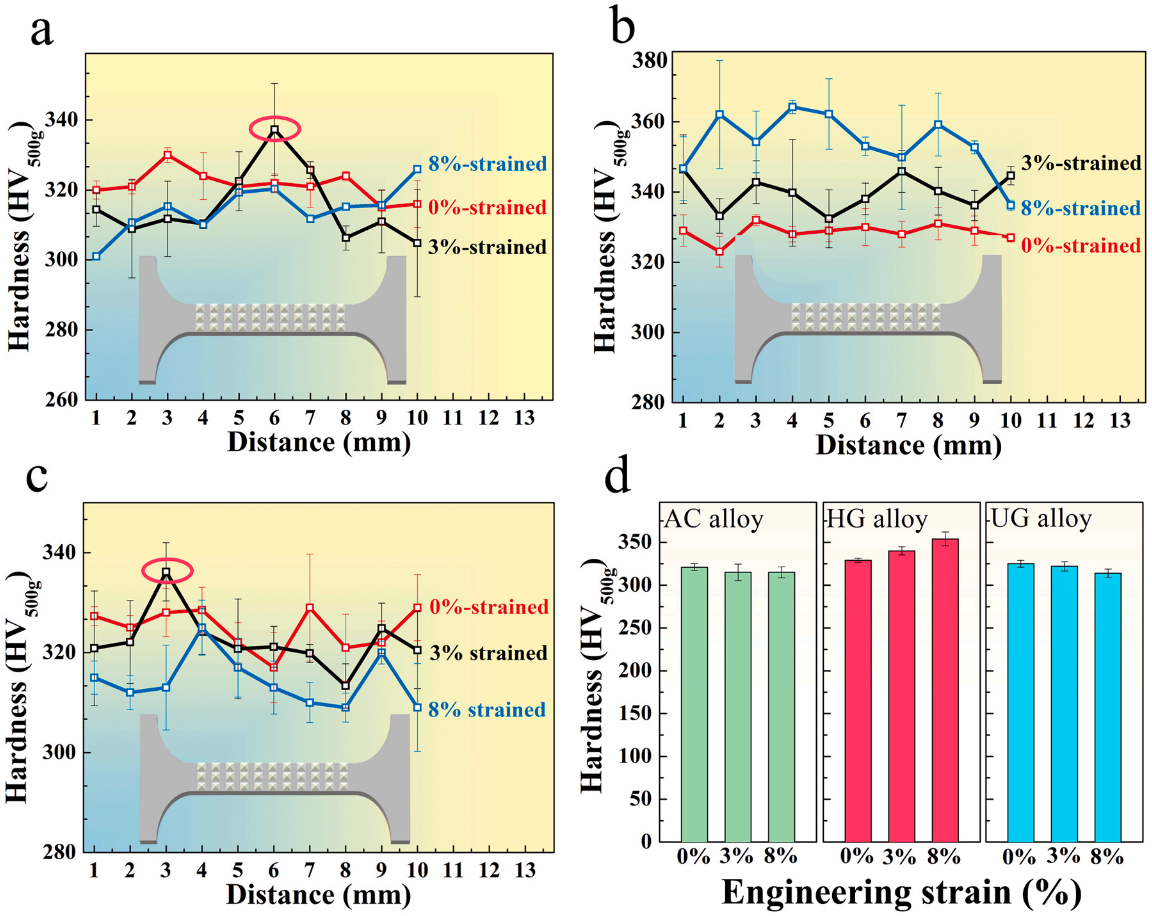

Fig. 4. The microhardness distributions for the three alloys under different strains. (a) AC specimen, (b) HG specimen, and (c) UG specimen. (d) The average microhardness of the different strained specimens.

conducted to explore the alloy's internal mechanisms, as hardness changes can indicate hardening behavior during deformation. Surprisingly, the HG specimen displayed unexpected deformation-induced continuous hardening, evident from the hardness-distribution map in Fig. 4b. Conversely, minimal hardening was observed for the AC and UG samples [Figs. 4(a, c)]. An abnormal trend was noted wherein hardness decreased with increasing strain for the AC and UG specimens, indicative of persistent dislocation-channel destruction during deformation, reducing dislocation-motion resistance and hardness (An et al., 2021). Notably, protruding points (marked as a red circle), potentially resulting from dislocation pile-up during deformation, were found in the 3 %-strained AC and UG specimens, signifying significant hardness differences due to localized deformation across the gauge section. Fig. 4d summarizes the average hardness for the three alloys at different tensile strains based on 30 indentations. The HG specimen exhibits persistent work hardening, presenting higher hardness at the same strain, compared to the other two alloys. For instance, the HG specimen's average hardness reaches 329 HV before deformation, exceeding the undeformed AC and UG alloys' average hardness of 321 HV and 325 HV, respectively (Fig. 4d).

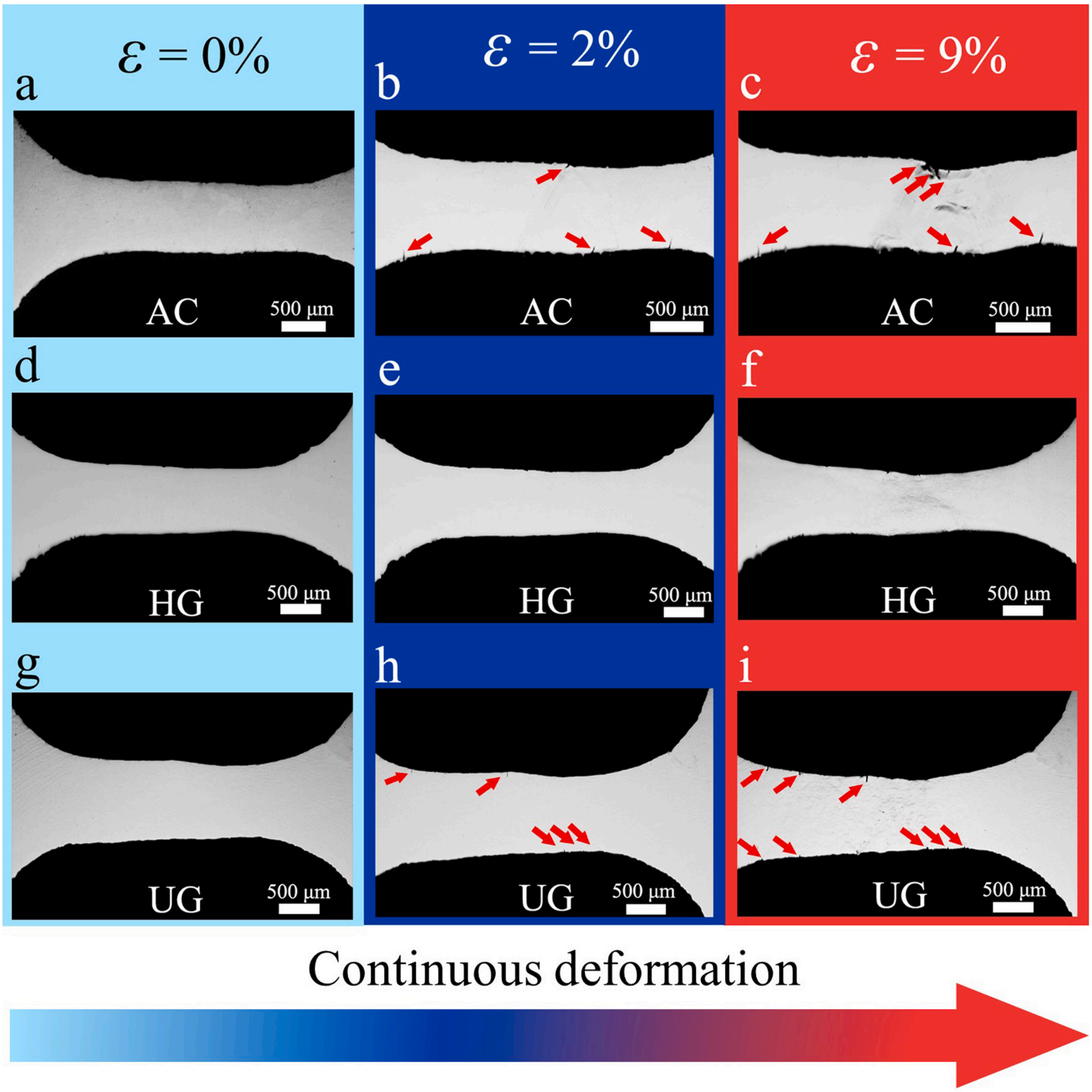

Fig. 5. Microstructural evolution of the three alloys with increasing strain. SEM in-situ tensile images of the AC alloy at (a) 0 % strain, (b) 2 % strain, and (c) 9 % strain. SEM in-situ tensile images of the HG alloy at (d) 0 % strain, (e) 2 % strain, and (f) 9 % strain. SEM in-situ tensile images of the UG alloy at (g) 0 % strain, (h) 2 % strain, and (i) 9 % strain. As evidenced by these direct observations, microcracking occurred in both the AC and UG alloys. On the contrary, no such microcracking was detected in the HG alloy, indicating that premature failure was successfully mitigated in the HG alloy.

3.3. Microstructural characterization after tensile testing

To understand the underlying deformation mechanisms closely, we conducted SEM in-situ tensile testing to observe the dynamic microstructural evolution in the three alloys. A premature failure phenomenon, characterized by the appearance of many microcracks, was observed on the pre-polished surface of the AC and UG alloys upon reaching the yield point [Figs. 5(b, h) and Supplementary movie 1]. Note that fewer but longer microcracks were observed on the AC sample than those on the UG sample at the initial stage of deformation. The cracks keep extending in length and width with increasing strains in the AC sample [Figs. 5(a - c)]. A profound necking morphology was found on the 9 %-strained AC sample, which is consistent with that on the ex-situ tensile sample, surrounded by large cracks (Fig. 5c). As compared, increasing strains resulted in persistent formation of microcracks with wide and short features in the UG sample [Figs. 5(g - i)]. Interestingly, no apparent microcrack was observed on the HG alloy until a 9 % strain [Figs. 5(d - f), and Supplementary movie 2], at which point the tensile stress begins to decline (Fig. 3a), indicating that the premature failure was avoided in the HG alloy.

The variation in grain size typically leads to distinct strain gradients during deformation. Geometrically necessary dislocations (GNDs) emerge around these zone boundaries to accommodate the strain gradients between grains, consequently altering lattice orientation (Zhu et al., 2021). The increased accumulation of dislocations leads to heightened interactions among dislocations in the alloy, where a higher GND density results in elevated back stresses, hence contributing to a higher $\sigma_{0.2}$ (Maity et al., 2018; Yang et al., 2016). EBSD, a robust method for measuring lattice orientation, is frequently utilized to gauge the GND density (Zhu et al., 2021). In Figs. 6(a - c), the EBSD IPF maps of the fractured AC, HG, and UG alloys reveal slightly elongated deformed grains towards the tensile direction in all samples. Colors in these IPF maps denote crystallographic orientations parallel to the tensile axis. The IPF maps of the HG alloy indicated that deformed grains favored orientations of $\langle 101\rangle$ and $\langle 001\rangle$ parallel to the tensile direction in this alloy. The $\langle 101\rangle$ and $\langle 001\rangle$ micro-textures are well-known deformation-texture modes in BCC HEAs (Abubaker Khan et al., 2022; Eleti et al., 2020).

This study employs the EBSD-Kernel Average Misorientation (KAM) method to assess localized misorientation from the EBSD-orientation data, frequently utilized to measure the GND density near zone boundaries in the three alloys (Calcagnotto et al., 2010). Continuous formation of GNDs was directly observed during the deformation in all three alloys using in-situ tensile testing (Supplementary Figs. 5 and 6). Corresponding to Figs 6(a - c), Figs 6(d - f) highlight the EBSD-KAM maps, with the inset in Fig. 6d illustrating the intensity bar for misorientation. Comparatively, the HG alloy exhibits more pronounced bright green and orange colors, signifying a higher degree of localized misorientation than the other alloys. Conversely, the AC alloy exhibits only slight green coloration, suggesting relatively minimal localized misorientation in this alloy. Furthermore, within the HG alloy, the orange color

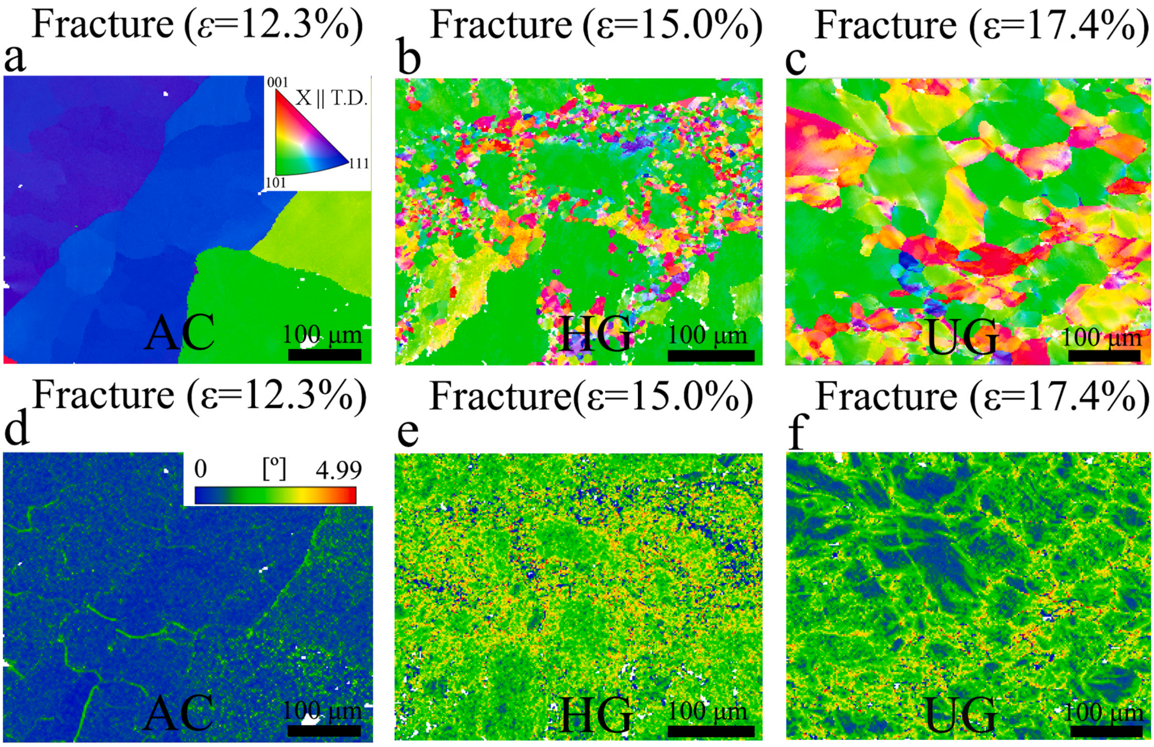

Fig. 6. Typical microstructures of deformed specimens. EBSD-IPF maps of the fractured (a) AC specimen, (b) HG specimen, and (c) UG specimen. Colors in the IPF maps correspond to crystallographic orientations parallel to the deformation direction according to the key stereographic triangle shown in the inset of image a. The deformation direction is parallel to the horizontal direction of the microstructures. The EBSD-Kernel Average Misorientation maps of the deformed (d) AC, (e) HG, and (f) UG specimens, which correspond to Fig. (a-c), respectively.

primarily concentrates along the boundary of fine-grain and coarse-grain zones, rather than consistently within either zone. This distribution suggests that the heterogeneous grain structure introduces more dislocations into the deformed alloy. Typically, the GND-density information can be calculated, using the following equation:

$$p_{GNDs} = \frac{2KAM_{ave}}{ub}, \tag{1}$$

where p_{GNDs} is the GND density in the aera of interest, $KAM_{(ave)}$ is the average localized misorientation measured by EBSD, b is the magnitude of the Burgers vector, u represents the inter-distance between the closest two detection points during EBSD analysis (Calcagnotto et al., 2010). The Burgers vector' modulus can be calculated according to Equations (2):

$$\parallel b \parallel = \frac{a_0\sqrt{h^2+k^2+l^2}}{2}, \tag{2}$$

where a_0 is the lattice constant of the tested specimen and can be obtained from the XRD result (Nutor et al.). The KAM_{ave} values are 0.6081 °, 2.3491 °, and 1.7631 ° for the AC, HG, and UG alloys, respectively. The calculated p_{GNDs} of the three samples are 0.260, 1.620 and 1.302 $\times$ 10^{14} m^{-2}, respectively. This is that more dislocations are stored in the deformed HG alloy.

The microstructural evolution during deformation for the three alloys at various engineering strains was further thoroughly investigated using the TEM characterizations. In Figs. 7(a, c), STEM bright-field (STEM-BF) micrographs of the 3 %-tensile-strained AC

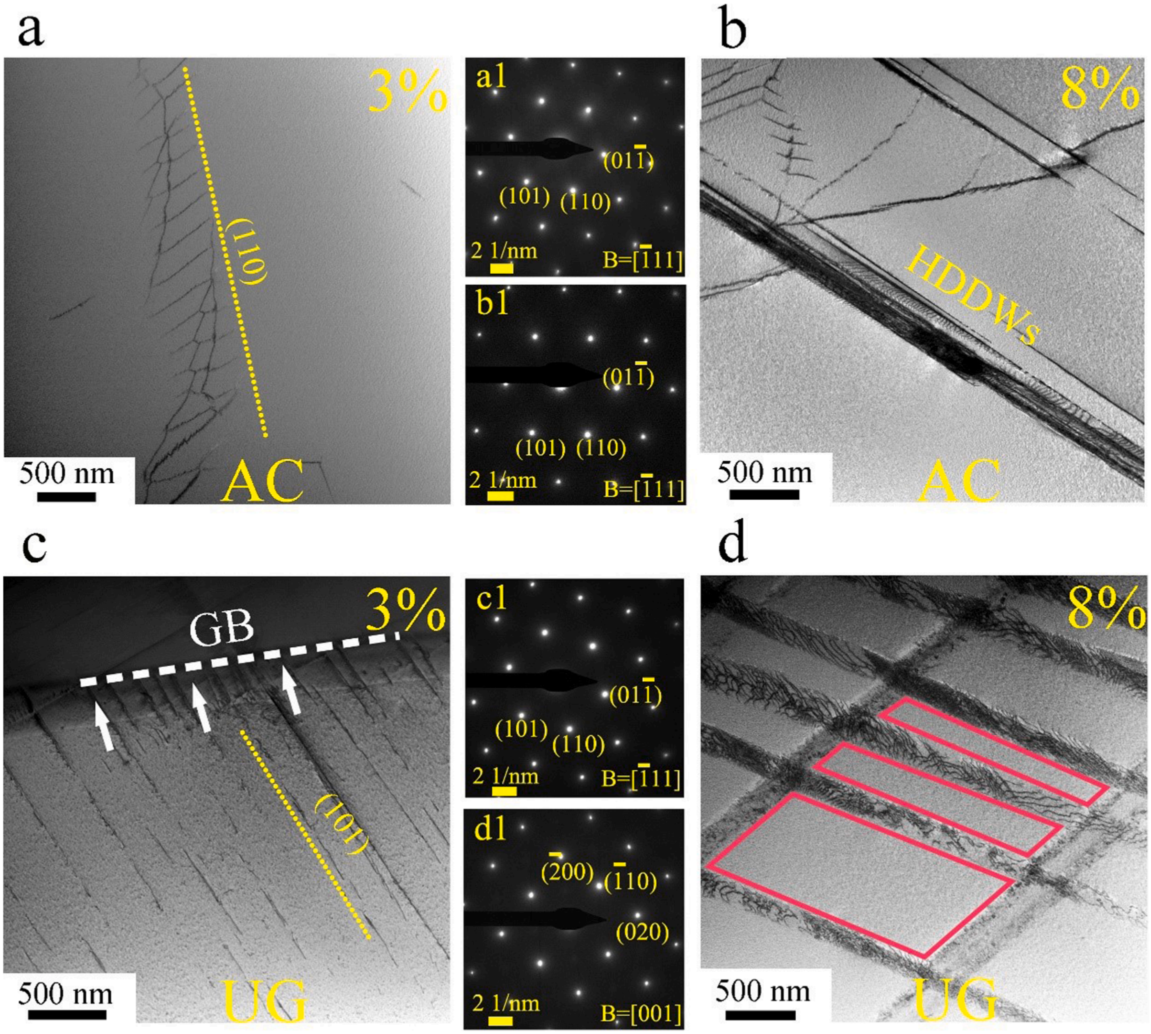

Fig. 7. Microstructural characterization of the deformed specimens. TEM images under the STEM-BF mode of the 3 %-strained specimens, (a) AC, and (c) HG specimens. The corresponding TEM SAED images of the 3 %-strained specimens, (a1) AC and (c1) UG specimens. TEM images under the STEM-BF mode of the 8 %-strained specimens, (b) AC, and (d) UG specimens. The corresponding TEM SAED images of the 8 %-strained specimens, (b1) AC and (d1) UG specimens. The red boxes sign part of the regions which have not undergone pronounced plastic deformation.

and UG alloys are presented. Both the AC (Fig. 7a) and UG specimens (Fig. 7c) exhibit numerous well-developed HDDWs activated during plastic deformation, terminating at grain boundaries. The planar slip of dislocations with mixed character on the {110}<111> slip system dominated the initial-stage plastic strain of AC and UG alloys [Figs. 7(a, c), Supplementary Fig. 7 and Supplementary Table 1]. Notably, the BCC structures of these two alloys remained unchanged during deformation, as evidenced by the SAED patterns [Figs. 7(a1, c1)]. It is worth noting that relatively few dislocations, as well as HDDWs, were observed in the AC specimen (Fig. 7a) at the same strain, compared to the UG alloy (Fig. 7c).

In the 3 %-tensile-strained HG specimen, an unusual presence of populated DCs, averaging 295 nm in diameter, emerged — an unprecedented observation within BCC-structured HEAs (Fig. 8a). These DCs exhibited substantial dislocation decoration along their cell walls, while the cell interiors displayed fewer dislocations with wavy or curved morphologies. Additionally, the specimen displayed distinct features, such as significant dislocation debris (marked as white arrows) and loops (marked as red arrows), indicating concentrated dislocation interactions or cross slips of screw dislocations within these DCs (Fig. 8c) (Li et al., 2023). Multiple Burgers vectors, including 1/2[111], 1/2[$\bar{1}$11], and 1/2[001], were identified in the 3 %-strained HG alloy, which contrasts with deformation mechanisms that are predominantly governed by a single slip system in the other two alloys (Supplementary Fig. 8). The increased critical stress required to move multiple types of dislocations contributed to the elevated material strength. Note that neither deformation-induced twinning nor phase transformation was observed in the deformed HG sample, as evidenced by SAED analysis (Fig. 8a1), signifying the predominant role of dislocation motion in coordinating the deformation process.

At an 8 %-tensile strain, a notable increase in the dislocation density within the DCs of the HG specimen was observed, along with the detection of fine-equiaxed DCs or dislocation lines within the larger DCs (Fig. 8b). Additionally, more HDDWs with narrow spatial distances were evident in the 8 %-strained HG specimen, indicative of sustained dislocation activation or propagation during deformation [Figs. 8(b, d)]. Concurrently, dislocation networks and multiple non-coplanar slip systems were activated with continuous deformation in the AC and UG specimens [Figs. 7(b, d)]. Notably, a specific region in Figs. 7(b, d) (highlighted in a red square), beyond

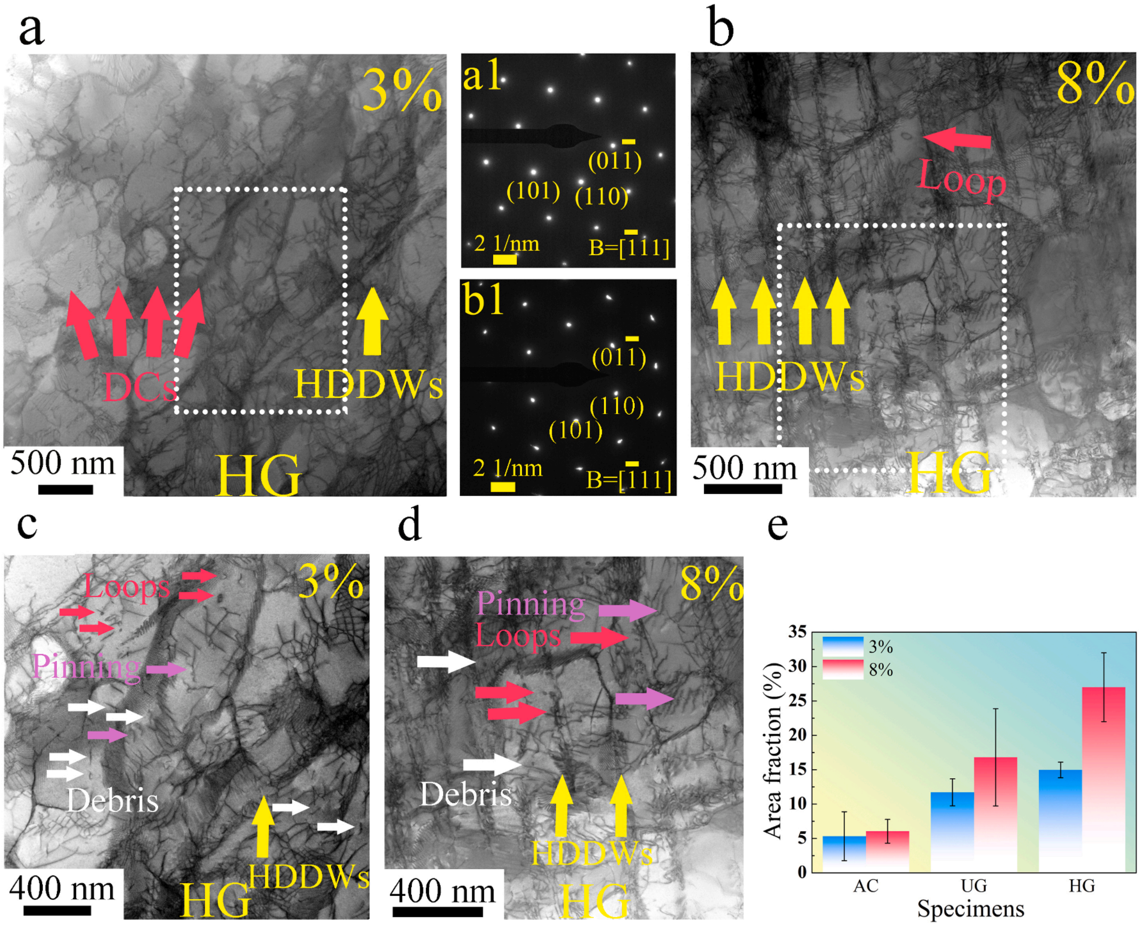

Fig. 8. Microstructural characterization of deformed HG specimens. (a) TEM image under the STEM-BF mode of the 3 %-strained specimen. (a1) The corresponding SAED image of the 3 %-strained specimen. (b) TEM image under the STEM-BF mode of the 8 %-strained specimen. (b1) The corresponding SAED image of the 8 %-strained specimen. The enlarged interesting area (c) corresponds to the white square in image (a), and (d) corresponds to the white square in image (b). (e) The areal fractions of the dislocations regions in the strained AC, HG, and UG alloys.

the HDDWs, showed minimal pronounced plastic deformation, lacking detected dislocations - a contrast to the equivalent region in the HG sample. Fig. 8e summarizes the areal fraction (F) of the deformed region in these specimens at 3 %- and 8 %-tensile strains. At the 3 % strain for the HG specimen, the DCs represented the predominant component of F, accounting for approximately 15 %, significantly surpassing the UG (12 %) and AC (5 %) specimens. The gradual increase in F for the HG specimen, attributed to refined DCs and emerging HDDWs, escalated to over 27 % at the 8 %-tensile strain. This augmentation in dislocations significantly contributed to the heightened tensile strength and average hardness of the specimen. Conversely, the increment in F for the other two specimens remained limited, reflecting prevalent localized deformation. At the 8 %-tensile strain, the F values were approximately 6 % and 17 % for the AC and UG specimens, respectively.

4. Discussion

4.1. *Deformation mechanisms*

A schematic diagram, based on the observed microstructural evolution, has been constructed to illustrate the typical plastic-deformation mechanisms observed in the three specimens. As illustrated in Figs. 7 and 8, dislocation motion is the primary deformation carrier during plasticity deformation in the three samples. In contrast to prevalent observations in other single-phase BCC HEAs, the HG specimen exhibited the presence of dense DCs at the initial stage of deformation, as depicted in Fig. 9a. This unique dislocation arrangement primarily stems from numerous dislocations activated during deformation and associated intensive multislip full dislocation interactions under a complex gradient stress-strain state during tensile deformation (Pan et al., 2021; Zhu et al., 2021). Here we explain the formation mechanism of the novel DC structure. The number of dislocations and associated interactions have significant impacts on both the formation of DC, $\sigma_{0.2}$, and post-yielding behaviors. Three primary reasons lead to the profuse dislocations in the HG sample. Firstly, the high intergranular stress and deformation compatibility among grains make grain boundaries the primary dislocation source at the initial stage of plasticity strain. Note that there are more dislocation sources (i.e., grain boundaries) in the HG sample compared to the other two samples due to the smaller grain size. Secondly, the heterogenous microstructure (Fig. 2 and Supplementary Fig. 2) resulting in the strain differences between the interface of fine grains and CGs during deformation in the HG sample. More GNDs were activated with increasing strains to accommodate the strain gradients between grains (Fig. 6, Supplementary Fig. 6). Thirdly, in addition to profuse dislocation sources and GNDs, multiple slip systems were activated by the gradient strain within individual grains [Figs. 8(a, c) and supplementary Fig. 8] to accommodate the plastic strain and strain incompatibility (Zhang et al., 2024). This activation of multiple-slip systems is in stark contrast with the single slip system in common uniform BCC HEAs, which favors the formation of DC structures. Additionally, indications of dislocation interactions or cross slips, such as dislocation loops and debris, were evident in the HG specimen (Fig. 9a). The profuse dislocations [Supplementary Figs. 9(d, e)], which are less observed in the other two samples [Supplementary Figs. 9 (a, b, c, d)], along with their interactions, significantly enhance the glide resistance the subsequent dislocations face. This salient hardening made the ongoing planar-slip unstable for surrounding dislocations and contributed to the activation of additional dislocations due to the accumulated local distortion. In particular, the cross-slip is encouraged by the elevated stress. A more severe lattice distortion than that in the other two alloys gradually formed in the HG alloy with frequent dislocation interaction (Supplementary Fig. 9f). Especially, the abundant dislocation loops resulting from cross-slip, not only contribute to the elevated glide resistance for subsequent dislocations, but also are more ready to promote dislocation proliferation as an effectively Frank-Ready dislocation source (Lei et al., 2018; Smith et al., 2020). These dislocations keep moving under an

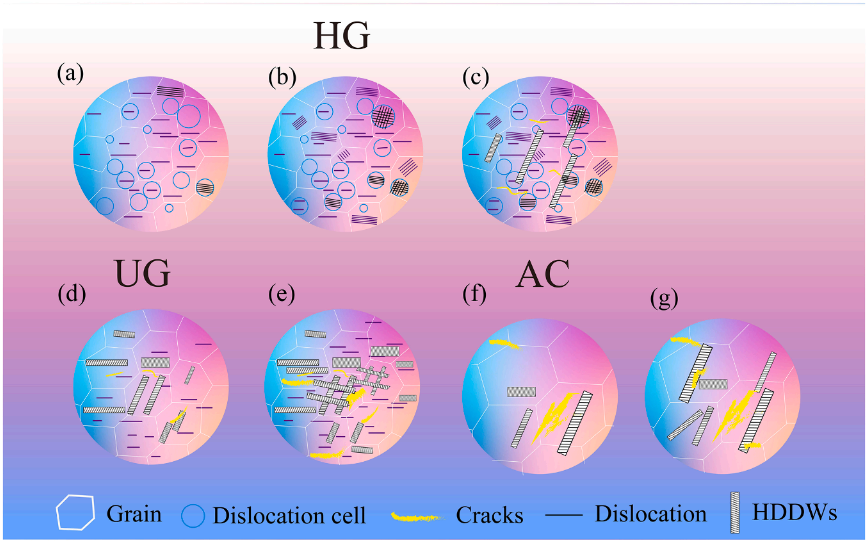

Fig. 9. Schematic diagram illustrating the plastic-deformation mechanisms of the three alloys: (a-c) HG alloy, (d, e) UG alloy, (f, g) AC alloy.

applied stress until they are blocked by elemental segregation on cell walls (Supplementary Fig. 10). These fluctuations in element concentration are stark characterize of the HEAs (Chen et al., 2021; Ding et al., 2019; Shuang et al., 2024). Note that the strain difference among grains of different sizes persists throughout the deformation process, extending with increasing strains. More GNDs and accompanied low angle grain boundaries (LAGBs) were formed (Supplementary Fig. 6) during this process. The GNDs contributed to the elevated hardening ability by long-range back stresses. Also, the LAGBs not only serve as dislocation sources emitting gliding dislocations, but also elevated dislocation motion resistance (Hao et al., 2020; Shi et al., 2024). In a nutshell, the activation of multiple slip systems, continuous generation of dislocations, accumulated strain difference, and related nonlocal strengthening resulted in the superior UTD and WHA of the HG sample.

The distinct substructure observed in the HG alloy significantly contributes to its exceptional UTD and work-hardening capability. Firstly, the wide dispersion of DCs at the initial stage of deformation in the HG specimen plays a crucial role in delaying the appearance of HDDWs, effectively suppressing plastic localization. Secondly, the boundaries of these DCs, rich in dislocations, serve as abundant sources for nucleating partial dislocations, engaging more dislocations in the deformation (Khan and Liu, 2016; Pan et al., 2021). Additionally, these cell boundaries confine newly formed dislocations within each cell, effectively mitigating severe stress concentrations caused by extensive dislocation pileups (Fig. 9b). Thirdly, the dense DCs induce an atomic-strain field significantly larger than that resulting from the composition fluctuation, leading to dynamic hardening when HDDWs traverse these regions (Fig. 9c). Note that some of HDDWs were overlapping with DC walls with increased strains (Fig. 8b). This overlapping results in a larger stress concentration compared to that induced by sole HDDWs in the entire sample. Ultimately, cracks initiated by the serious stress concentrations induced by the combination of HDDWs and cell walls propagate rapidly until they interfere with each other (Fig. 9c), culminating in a sample failure. This caused a relatively low degree of elongation of fracture for the HG sample compared to the UG sample (Fig. 3a).

Conversely, narrow HDDWs with stress concentrations and dislocation debris govern the deformation at the early stage in the other two specimens [Figs. 9(d, f)]. Grain boundaries serve as the primary dislocation sources for the AC and UG samples during the initial stages of deformation due to their uniform microstructure. This trend contrasts sharply with the multiple dislocation sources in the HG sample. Moreover, compared with the HG sample, the other two samples exhibited a reduced grain boundary area fraction due to their larger grain sizes. Therefore, the number of HDDWs in the AC specimen is notably fewer than in the UG alloy. The initial dislocations within HDDWs diminish the glide resistance for subsequent dislocations, promoting 'sliding-plane softening,' favoring planar slip and infrequent cross-slip (An et al., 2021). As anticipated from the reduced dislocation-motion resistance, the engineering stress-strain curve exhibited minimal work-hardening capability and UTD (Fig. 3a). A critical consequence of HDDWs in the AC and UG specimens is the severe stress concentration at grain boundaries, where is known for poor adhesion due to impurity elemental concentration or solidification defects (Wang et al., 2022). This feature severe stress concentration, combined with poor adhesion, contributes to crack initiation near grain boundaries and premature failure in these specimens [Figs. 9(d, f)]. The relatively fine and uniform grain size could deflect crack paths, which resulted in the decreased local crack-driving force at the crack tip and buffer the crack extension (Cao et al., 2020; Li et al., 2022b; Shi et al., 2021). Consequently, the UG alloy exhibits more cracks with shorter lengths and uniform widths in comparison to the AC alloy.

The continued deformation activates more dislocations along the planar-slip band, characterized by the minimal motion resistance, leading to the rapid saturation of dislocation accumulation within HDDWs. Consequently, new slip planes are activated, expanding the deformation area, and enhancing ductility in these specimens [Figs. 9(e, g)]. However, despite the enhanced interaction between dislocations contributing to the increased ductility, it makes a limited contribution to the ultimate strength due to continuous crack propagation. The stress-strain curves exhibit rapid and steep declines when the dislocation-motion resistance fails to neutralize stress reduction caused by crack propagation in the final stages of deformation (Fig. 3a).

4.2. *Strengthening mechanisms*

There are many strengthening mechanisms, including the solid-solution strengthening ($\Delta\sigma_{ss}$), estimated inherent $\sigma_{0.2}$ of the alloy component [$\Delta(\sigma_{0.2})_{mix}$], grain-boundary strengthening ($\Delta\sigma_{gb}$), and dislocation strengthening ($\Delta\sigma_d$), which result in a high $\sigma_{0.2}$ of these single-phase polycrystalline metals and alloys with uniform microstructures. Additionally, an effectively hetero-deformation inducing (HDI) hardening (σ_{HDI}) would also form in UG and HG alloys, resulting from distinct strain gradients during deformation (Qin et al., 2022; Yang et al., 2016). The $\sigma_{0.2}$ for these alloys can be expressed by the following formula:

$$\sigma_{0.2} = \Delta(\sigma_{0.2})_{mix} + \Delta\sigma_{ss} + \Delta\sigma_{gb} + \Delta\sigma_d + \sigma_{HDI}. \tag{3}$$

4.2.1. *Strength from alloy component*

The $\Delta(\sigma_{0.2})_{mix}$ can be obtained according to the rule of mixing (ROM), which can be expressed as the following formula:

$$\Delta(\sigma_{0.2})_{mix} = c_i(\sigma_{0.2})_i, \tag{4}$$

where c_i is the mole content of the *i*th constituent element, and the $(\sigma_{0.2})_i$ is the $\sigma_{0.2}$ of the *i*th constituent element, respectively. Supplementary Table 2 listed the $\Delta\sigma_{0.2}$ of the constituent elements. Alloys having identical chemical compositions have the same levels of component strengthening, and the computed $\Delta(\sigma_{0.2})_{mix}$ for all the AC, HG, and UG alloys are 230 MPa.

4.2.2. *Solid-solution strengthening*

Elastic interactions between the localized stress field of the solute atoms and the localized stress field of the dislocations result in the solid-solution strengthening of a BCC-structured HEA (Fleischer, 1963; Gypen and Deruyttere, 1977; Senkov et al., 2011a). The $\Delta\sigma_{ss}$ can be described by the following equation:

$$\Delta\sigma_{ss} = \left(\sum (\Delta\sigma_i)^{3/2}\right)^{2/3}, \tag{5}$$

where $\Delta\sigma_i$ is the contribution of the ith element in terms of solid-solution strengthening. $\Delta\sigma_i$ can be calculated as follows:

$$\Delta\sigma_i = AGf_i^{4/3}c_i^{2/3}, \tag{6}$$

where A is a materials-dependent dimensionless constant and can be taken as 0.04 for the BCC-structured HEAs (Senkov et al., 2011a). G is the shear modulus of the alloy and can be calculated from the ROM. The f value is defined by the following equation:

$$f_i = \sqrt{\delta_{G,i}^2 + \alpha^2\delta_{r,i}^2}, \tag{7}$$

$$\delta_{r,i} = \frac{9\sum c_j\delta_{r,ij}}{8}, \tag{8}$$

$$\delta_{G,i} = \frac{9\sum c_j\delta_{G,ij}}{8}, \tag{9}$$

where $\delta_{G,i}$ is the shear modulus misfit, and $\delta_{G,i}$ is composed of the atomic-size misfit. Also, $\delta_{r,ij}$ and $\delta_{G,ij}$ are the atomic-radius difference and the shear-modulus difference between the ith and jth elements, respectively, where α is a constant and depends on the dislocation types. α is taken in the range of 2 – 4 for screw dislocations and taken as 16 for edge dislocations. Here α has been taken to be 9 for the three alloys as both dislocations were observed in them (Supplementary Figs. 7 and 8) (Senkov et al., 2011a). The presence of both screw and edge dislocations in the present BCC-structured alloys is in agreement with the literature (Feng et al., 2021; Lee et al., 2020, 2021; Wang et al., 2020). The atomic-radius difference and the shear-modulus difference can be described as follows:

$$\delta_{r,ij} = \frac{2(r_i - r_j)}{r_i + r_j}, \tag{10}$$

$$\delta_{G,ij} = \frac{2(G_i - G_j)}{G_i + G_j}, \tag{11}$$

The $\sigma_{0.2}$, atomic radius (r), and shear modulus (G) of the constituent elements are given in Supplementary Table 2. As previously discussed, the influence of solid-solution strengthening in a single-phase BCC-structured HEA relies on chemical composition. Alloys sharing identical chemical compositions yield equivalent levels of solid-solution strengthening. Based on Eqs. (5-11), the computed $\Delta\sigma_{ss}$ for all the AC, HG, and UG alloys amounted to 710 MPa.

4.2.3. *Grain-boundary strengthening*

As shown in Fig. 7, the grain boundary has a strong effect in hindering the movement of the dislocation, resulting in a high strength. The contribution of grain-boundary strengthening to $\sigma_{0.2}$ can be calculated, using the Hall-Petch equation:

$$\sigma_{gb} = k_s d^{(-1/2)}, \tag{12}$$

where k_s is the Hall-Petch strengthening coefficient and is taken as 270 MPa•μm$^{0.5}$ in some works (Chen et al., 2019; Juan et al., 2016), and d is the average grain size. Obviously, a smaller grain size would lead to a higher grain-boundary strengthening effect. The calculated σ_{gb} values are 13 MPa, 152 MPa, and 54 MPa for the AC, HG, and UG alloys, respectively.

4.2.4. *Dislocation strengthening*

As an important deformation medium, dislocation motion carried the plastic flow under the influence of an applied stress. Interactions of dislocations hiding their further movement essentially require a higher applied stress to keep the plastic flow going, resulting in a greater tensile strength (Li et al., 2021). The Taylor hardening formula [Eq. (13)] is used to describe the contribution of dislocation strengthening to strength (Ganji et al., 2017):

$$\sigma_d = Ma_T Gbp^{1/2}, \tag{13}$$

where the M is the Taylor constant and is suggested to be 5 in some conventional BCC Ti alloys and BCC HEAs (Wang et al., 2023c). The a_T is a constant that depends on the type of materials, i.e., ranging from 0.3 – 0.5 and is taken as 0.4 in the present work (Ungár et al., 2014). G is the shear modulus of alloys. b is the magnitude of the Burgers vector, which can be calculated as $\| b \| = \frac{a_0\sqrt{h^2+k^2+l^2}}{2}$, where a_0 is the lattice constant and can be calculated from XRD. The crystal plane with the highest intensity in the XRD patterns was used to calculate the lattice constant as well as $\| b \|$ for the samples (Nutor et al., 2021; Zhu and Starke, 1999). p is the dislocation density, which is expressed by the following formula:

$$p = \frac{2\sqrt{3}\varepsilon}{db}, \tag{14}$$

where the ε is the microstrain that estimated from the XRD results of deformed samples according to the Williamson-Hall method (Khorsand Zak et al., 2011; Nutor et al., 2021). The grain size, d, crystal plane with the highest intensity, (h, k, l), lattice constant, a_0, microstrain, ε, and shear modulus of the alloys are listed in Supplementary Table 3. Therefore, the dislocation-strengthening contributions, σ_d, are 1 MPa, 16 MPa, and 4 MPa for the AC, HG, and UG alloys, respectively.

4.2.5. Hetero-deformation inducing strengthening

The σ_{HDI} resulting from the plastic-deformation incompatibility can be obtained by the combination of LUR curves (Supplementary Fig. 11) and following formulas (Shi et al., 2024; Yang et al., 2016; Zhu and Wu, 2019):

$$\sigma_B = \frac{\sigma_r + \sigma_u}{2} \tag{15}$$

$$\sigma_E = \sigma_p - \sigma_B \tag{16}$$

where σ_r and σ_u is the unloading yield stress and reloading yield stress, respectively. The σ_p is the stress at the beginning of unloading. A point is considered to represent the yield point when its slope is 5 % less than the effective elastic modulus (Wang et al., 2023b). The calculated σ_{HDI} is 104 MPa and 60 MPa for the HG and UG samples, respectively. While the σ_{HDI} for the AC sample is not calculated here because the sample fractured during the LUR tests due to serious premature failure, it is believed that HDI hardening has almost no contribution to strength in the AC sample as only a few GNDs (eighth of that in the HG sample) was detected in the AC sample (Fig. 6 and supplementary Fig. 5).

The schematic diagram compared the estimated theoretical $\sigma_{0.2}$ and the experimental $\sigma_{0.2}$ of the three alloys, indicating the model can capture the magnitude and help understand the underlying mechanisms (Supplementary Fig. 12). Specifically, Table 1 summarizes the contribution values stemming from different strengthening mechanisms of the three samples. Although solid-solution strengthening and contributions from alloy components serve as the predominant strengthening mechanisms, grain-boundary strengthening, and HDI hardening also make substantial contributions to their enhanced strength. This trend implies that microstructural strategies aimed at achieving a finer grain size and more heterogeneous structures could improve the strength effectively of BCC-structured HEAs.

While the DC structure and associated strengthening mechanism effectively elevated the alloy's UTD and strength under quasi-static loading conditions, additional work is needed in the future to determine whether this enhancement effect can be applied under more harsher environments, such as under dynamic-loading conditions. It is believed that the competition between dislocation-mediated plasticity and grain boundary-mediated plasticity determines the mechanical properties of alloys under dynamic-loading conditions. To start with, note that other defects, such as twins, stacking faults, and phase transition, are less likely to form in the three alloys due to their high stacking-fault energies, which is in stark contrast to what is observed in the FCC HEA (He et al., 2018). Under conditions where dislocation motion dominates plastic strain, the activation of numerous dislocations sharply enhances dislocation interactions, resulting in an elevated hardness for the three samples. However, the abrupt and substantial surge in stress-induced dislocations aggressively overcomes obstacles resulted from elemental segregation, causing a poor UTD (Supplementary Fig. 13). Additional GNDs would be activated in line with the applied strain in the HG sample. The combination of the above factors makes for a higher hardness increment for the HG sample than for the other two samples. However, the serious stress concentration would lead to decreased strains for all the samples.

Things change when grain boundary-mediated deformation becomes the prevalent deformation process at a higher strain rate. High temperatures, resulting from the thermal effect of high-speed plastic deformation (Xie et al., 2022), promote dislocation annihilation and GB sliding, leading to a decreased strength and hardness compared to those for the three samples under quasi-static conditions. Furthermore, the DC structure and associated UTD are hard to detect because of promoted dislocation annihilation, which lowers the hardness difference between the UG and HG samples.

The proposed models effectively elucidate the strengthening mechanisms under quasi-static loading conditions and serve as valuable tools for guiding alloy design and processing in such environments. However, their efficacy is limited in accurately revealing the strain-rate sensitivity and mechanical behavior post-yield. A theoretical model, such as one based on dislocation-density-based crystal plasticity (Agaram et al., 2021; Cappola et al., 2024; Fischer et al., 2024; Li et al., 2024) that incorporates various deformation mechanisms, should be developed to accurately capture the mechanical behavior under diverse-loading scenarios. This feature can provide valuable reference to obtain a better property for applications involving multiple conditions.

Table 1

A summary of strength contribution from solid-solution strengthening [$\Delta\sigma_{SS}$, (MPa)], strength from alloy component [$\Delta(\sigma_{0.2})_{mix}$, (MPa)], grain-boundary strengthening [$\Delta\sigma_{gb}$, (MPa)], and hetero-deformation inducing strengthening [$\Delta\sigma_{HDI}$, (MPa)] for the three samples.

Samples	$\Delta\sigma_{SS}$	$\Delta(\sigma_{0.2})_{mix}$	$\Delta\sigma_{gb}$	$\Delta\sigma_d$	$\Delta\sigma_{HDI}$	Sum
AC	710	230	13	1		954
HG	710	230	152	16	104	1212
UG	710	230	54	4	60	1058

5. Conclusions

In summary, we have not only proposed a solution to the long-standing issue of poor UTD in BCC HEAs without compromising $\sigma_{0.2}$ (in fact, resulting in its elevation), but we have also uncovered a completely new deformation mechanism based on a heterogeneous grain-size structure. The current findings present us with an evolution of the activation of slip systems and amplified dislocation interactions, leading to significantly improved UTD (by 349.1 %) and effectively suppressing premature failure. Specifically, the single-phase BCC HEA achieves a room-temperature $\sigma_{0.2}$ of 1200 MPa and a UTD of ~ 8 % (with 15 % elongation-to-failure), surpassing nearly all reported ductile BCC HEAs. More relevantly, we are convinced that our strategy is urgently needed within the BCC-alloy community and is well-appropriate to be adopted by other HEA systems. This approach will contribute significantly to achieving better mechanical properties and improving their safety, which is essential for advancing the industrial application of this kind of alloy, such as thermal-power stations and aerospace systems.

CRediT authorship contribution statement

Rui Huang: Writing – original draft, Visualization, Validation, Methodology, Investigation, Formal analysis, Data curation, Conceptualization. **Lingkun Zhang:** Formal analysis, Data curation. **Abdukadir Amar:** Validation, Formal analysis, Data curation. **Peter K. Liaw:** Writing – review & editing, Funding acquisition, Conceptualization. **Tongmin Wang:** Supervision, Formal analysis. **Tingju Li:** Supervision, Methodology. **Yiping Lu:** Writing – review & editing, Supervision, Resources, Project administration, Funding acquisition, Formal analysis.

Declaration of competing interest

The authors declare that they have no known competing financial interests or personal relationships that could have appeared to influence the work reported in this paper.

Data availability

The data that support the findings of this study are available from the corresponding author upon request.

Acknowledgements

This work was supported by the National Natural Science Foundation of China (Nos U20A20278 and U2341261). PKL very much appreciates the support from (1) the National Science Foundation (DMR – 1611180, 1809640, and 2226508) and (2) the Army Research Office (W911NF-13–1–0438, and W911NF-19–2–0049, and FA9550–23–1–0503).

Supplementary materials

Supplementary material associated with this article can be found, in the online version, at doi:10.1016/j.ijplas.2024.104079.

References

Abubaker Khan, M., Wang, T.L., Feng, C., Sun, H., Wang, B., Hamza, M., yasin, G., Afifi, M.A., Liao, W.B., 2022. A superb mechanical behavior of newly developed lightweight and ductile $Al_{0.5}Ti_2Nb_1Zr_1W_x$ refractory high entropy alloy via nano-precipitates and dislocations induced-deformation. Mater. Des. 222, 111034.

Agaram, S., Kanjarla, A.K., Bhuvaraghan, B., Srinivasan, S.M., 2021. Dislocation density based crystal plasticity model incorporating the effect of precipitates in IN718 under monotonic and cyclic deformation. Int. J. Plast. 141, 102990.

An, Z., Mao, S., Yang, T., Liu, C.T., Zhang, B., Ma, E., Zhou, H., Zhang, Z., Wang, L., Han, X., 2021. Spinodal-modulated solid solution delivers a strong and ductile refractory high-entropy alloy. Mater. Horiz. 8, 948–955.

Bahramyan, M., Mousavian, R.T., Brabazon, D., 2020. Study of the plastic deformation mechanism of TRIP–TWIP high entropy alloys at the atomic level. Int. J. Plast. 127, 102649.

Calcagnotto, M., Ponge, D., Demir, E., Raabe, D., 2010. Orientation gradients and geometrically necessary dislocations in ultrafine grained dual-phase steels studied by 2D and 3D EBSD. Mater. Sci. Eng. A 527, 2738–2746.

Cantor, B., Chang, I.T.H., Knight, P., Vincent, A.J.B., 2004. Microstructural development in equiatomic multicomponent alloys. Mater. Sci. Eng. A 213–218, 375-377.

Cao, R., Yu, Q., Pan, J., Lin, Y., Sweet, A., Li, Y., Ritchie, R.O., 2020. On the exceptional damage-tolerance of gradient metallic materials. Mater. Today 32, 94–107.

Cappola, J., Wang, J., Li, L., 2024. A dislocation-density-based crystal plasticity model for FCC nanocrystalline metals incorporating thermally-activated depinning from grain boundaries. Int. J. Plast. 172, 103863.

Chen, S., Tseng, K.K., Tong, Y., Li, W., Tsai, C.W., Yeh, J.W., Liaw, P.K., 2019. Grain growth and Hall-Petch relationship in a refractory HfNbTaZrTi high-entropy alloy. J. Alloys Compd. 795, 19–26.

Chen, X., Wang, Q., Cheng, Z., Zhu, M., Zhou, H., Jiang, P., Zhou, L., Xue, Q., Yuan, F., Zhu, J., Wu, X., Ma, E., 2021. Direct observation of chemical short-range order in a medium-entropy alloy. Nature 592, 712–716.

Chu, C., Chen, W., Huang, L., Wang, H., Chen, L., Fu, Z., 2024. Exceptional strength-ductility synergy at room and liquid nitrogen temperatures of $Al_{7.5}Co_{20.5}Fe_{24}Ni_{24}Cr_{24}$ high-entropy alloy with hierarchical precipitate heterogeneous structure. Int. J. Plast. 175, 103939.

Dasari, S., Sharma, A., Jiang, C., Gwalani, B., Lin, W.C., Lo, K.C., Gorsse, S., Yeh, A.C., Srinivasan, S.G., Banerjee, R., 2023. Exceptional enhancement of mechanical properties in high-entropy alloys via thermodynamically guided local chemical ordering. Proc. Natl. Acad. Sci. U.S.A. 120, e2211787120.

Ding, J., Yu, Q., Asta, M., Ritchie, R.O., 2018. Tunable stacking fault energies by tailoring local chemical order in CrCoNi medium-entropy alloys. Proc. Natl. Acad. Sci. U.S.A. 115, 8919–8924.

Ding, Q., Zhang, Y., Chen, X., Fu, X., Chen, D., Chen, S., Gu, L., Wei, F., Bei, H., Gao, Y., Wen, M., Li, J., Zhang, Z., Zhu, T., Ritchie, R.O., Yu, Q., 2019. Tuning element distribution, structure and properties by composition in high-entropy alloys. Nature 574, 223–227.

Eleti, R.R., Chokshi, A.H., Shibata, A., Tsuji, N., 2020. Unique high-temperature deformation dominated by grain boundary sliding in heterogeneous necklace structure formed by dynamic recrystallization in HfNbTaTiZr BCC refractory high entropy alloy. Acta Mater 183, 64–77.

Feng, R., Feng, B., Gao, M.C., Zhang, C., Neuefeind, J.C., Poplawsky, J.D., Ren, Y., An, K., Widom, M., Liaw, P.K., 2021. Superior high-temperature strength in a supersaturated refractory high-entropy alloy. Adv. Mater. 33, 2102401.

Fischer, T., Zhou, T., Dahlberg, C.F.O., Hedström, P., 2024. Relating stress/strain heterogeneity to lath martensite strength by experiments and dislocation density-based crystal plasticity. Int. J. Plast. 174, 103917.

Fu, W., Huang, Y., Sun, J., Ngan, A.H.W., 2022. Strengthening CrFeCoNiMn$_{0.75}$Cu$_{0.25}$ high entropy alloy via laser shock peening. Int. J. Plast. 154, 103296.

Fujita, N., Ishikawa, N., Roters, F., Tasan, C.C., Raabe, D., 2018. Experimental–numerical study on strain and stress partitioning in bainitic steels with martensite–austenite constituents. Int. J. Plast. 104, 39–53.

Ganji, R.S., Sai Karthik, P., Bhanu Sankara Rao, K., Rajulapati, K.V., 2017. Strengthening mechanisms in equiatomic ultrafine grained AlCoCrCuFeNi high-entropy alloy studied by micro- and nanoindentation methods. Acta Mater 125, 58–68.

George, E.P., Raabe, D., Ritchie, R.O., 2019. High-entropy alloys. Nat. Rev. Mater. 4, 515–534.

Gou, S., Gao, M., Shi, Y., Li, S., Fang, Y., Chen, X., Chen, H., Yin, W., Liu, J., Lei, Z., Wang, H., 2023. Additive manufacturing. of ductile refractory high-entropy alloys via phase engineering. Acta Mater 248, 118781.

Granberg, F., Nordlund, K., Ullah, M.W., Jin, K., Lu, C., Bei, H., Wang, L.M., Djurabekova, F., Weber, W.J., Zhang, Y., 2016. Mechanism of radiation damage reduction in equiatomic multicomponent single phase alloys. Phys. Rev. Lett. 116, 135504.

Gupta, A., Jian, W.R., Xu, S., Beyerlein, I.J., Tucker, G.J., 2022. On the deformation behavior of CoCrNi medium entropy alloys: unraveling mechanistic competition. Int. J. Plast. 159, 103442.

Hao, Y., Tan, C., Yu, X., Chen, R., Nie, Z., Ren, Y., Yang, S., Li, Y., Wang, F., 2020. Effect of grain boundary misorientation angle on diffusion behavior in molybdenum-tungsten systems. J. Alloys Compd. 819, 152975.

Hasan, M.N., Liu, Y.F., An, X.H., Gu, J., Song, M., Cao, Y., Li, Y.S., Zhu, Y.T., Liao, X.Z., 2019. Simultaneously enhancing strength and ductility of a high-entropy alloy via gradient hierarchical microstructures. Int. J. Plast. 123, 178–195.

Jeong, H.T., Kim, W.J., 2021. Microstructure tailoring of Al$_{0.5}$CoCrFeMnNi to achieve high strength and high uniform strain using severe plastic deformation and an annealing treatment. J. Mater. Sci. Technol. 71, 228–240.

Juan, C.C., Tsai, M.H., Tsai, C.W., Hsu, W.L., Lin, C.M., Chen, S.K., Lin, S.J., Yeh, J.W., 2016. Simultaneously increasing the strength and ductility of a refractory high-entropy alloy via grain refining. Mater. Lett. 184, 200–203.

Karthik, G.M., Kim, Y., Kim, E.S., Zargaran, A., Sathiyamoorthi, P., Park, J.M., Jeong, S.G., Gu, G.H., Amanov, A., Ungar, T., Kim, H.S., 2022. Gradient heterostructured laser-powder bed fusion processed CoCrFeMnNi high entropy alloy. Addit. Manuf. 59, 103131.

Kaushik, L., Kim, M.S., Singh, J., Kang, J.H., Heo, Y.U., Suh, J.Y., Choi, S.H., 2021. Deformation mechanisms and texture evolution in high entropy alloy during cold rolling. Int. J. Plast. 141, 102989.

Khan, A.S., Liu, J., 2016. A deformation mechanism based crystal plasticity model of ultrafine-grained/nanocrystalline FCC polycrystals. Int. J. Plast. 86, 56–69.

Khorsand Zak, A., Abd. Majid, W.H., Abrishami, M.E., Yousefi, R., 2011. X-ray analysis of ZnO nanoparticles by Williamson-Hall and size-strain plot methods. Solid State Sci 13, 251–256.

Kishore, K., Chandan, A.K., Hung, P.T., Kumar, S., Ranjan, M., Kawasaki, M., Gubicza, J., 2023. Effect of Si on the evolution of plasticity mechanisms, grain refinement and hardness during high-pressure torsion of a non-equiatomic CoCrMnNi multi-principal element alloy. Int. J. Plast. 169, 103720.

Kong, W., Cox, S.C., Lu, Y., Villapun, V., Xiao, X., Ma, W., Liu, M., Attallah, M.M., 2022. Microstructural evolution, mechanical properties, and preosteoblast cell response of a post-processing-treated TNT5Zr β Ti alloy manufactured via selective laser melting. ACS Energy Lett 8, 2336–2348.

Kumar, P., Michalek, M., Cook, D.H., Sheng, H., Lau, K.B., Wang, P., Zhang, M., Minor, A.M., Ramamurty, U., Ritchie, R.O., 2023. On the strength and fracture toughness of an additive manufactured CrCoNi medium-entropy alloy. Acta Mater 258, 119249.

Lee, C., Kim, G., Chou, Y., Musicó, B.L., Gao, M.C., An, K., Song, G., Chou, Y.C., Keppens, V., Chen, W., Liaw, P.K., 2020. Temperature dependence of elastic and plastic deformation behavior of a refractory high-entropy alloy. Sci. Adv. 6, eaaz4748.

Lee, C., Maresca, F., Feng, R., Chou, Y., Ungar, T., Widom, M., An, K., Poplawsky, J.D., Chou, Y.C., Liaw, P.K., Curtin, W.A., 2021. Strength can be controlled by edge dislocations in refractory high-entropy alloys. Nat. Commun. 12, 5474.

Lei, Z., Liu, X., Wu, Y., Wang, H., Jiang, S., Wang, S., Hui, X., Wu, Y., Gault, B., Kontis, P., Raabe, D., Gu, L., Zhang, Q., Chen, H., Wang, H., Liu, J., An, K., Zeng, Q., Nieh, T.G., Lu, Z., 2018. Enhanced strength and ductility in a high-entropy alloy via ordered oxygen complexes. Nature 563, 546–550.

Li, J., Xu, Y., Xiao, W., Ma, C., Huang, X., 2022. Development of Ti-Al-Ta-Nb-(*Re*) near-α high temperature titanium alloy: microstructure, thermal stability and mechanical properties. J. Mater. Sci. Technol. 109, 1–11.

Li, T., Wang, S., Fan, W., Lu, Y., Wang, T., Li, T., Liaw, P.K., 2023. CALPHAD-aided design for superior thermal stability and mechanical behavior in a TiZrHfNb refractory high-entropy alloy. Acta Mater 246, 118728.

Li, W., Xiang, M., Aitken, Z.H., Chen, S., Xu, Y., Yang, X., Pei, Q., Wang, J., Li, X., Vastola, G., Gao, H., Zhang, Y.W., 2024. Unraveling the Hall-Petch to inverse Hall-Petch transition in nanocrystalline high entropy alloys under shock loading. Int. J. Plast. 178, 104010.

Li, W., Xie, D., Li, D., Zhang, Y., Gao, Y., Liaw, P.K., 2021. Mechanical behavior of high-entropy alloys. Prog. Mater. Sci. 118, 100777.

Lilensten, L., Couzinié, J.P., Bourgon, J., Perrière, L., Dirras, G., Prima, F., Guillot, I., 2017. Design and tensile properties of a bcc Ti-rich high-entropy alloy with transformation-induced plasticity. Mater. Res. Lett. 5, 110–116.

Liu, L., Zhang, Y., Li, J., Fan, M., Wang, X., Wu, G., Yang, Z., Luan, J., Jiao, Z., Liu, C.T., Liaw, P.K., Zhang, Z., 2022b. Enhanced strength-ductility synergy via novel bifunctional nano-precipitates in a high-entropy alloy. Int. J. Plast. 153, 103235.

Ma, E., Wu, X., 2019. Tailoring heterogeneities in high-entropy alloys to promote strength–ductility synergy. Nat. Commun. 10, 5623.

Madivala, M., Schwedt, A., Prahl, U., Bleck, W., 2019. Anisotropy and strain rate effects on the failure behavior of TWIP steel: a multiscale experimental study. Int. J. Plast. 115, 178–199.

Madivala, M., Schwedt, A., Wong, S.L., Roters, F., Prahl, U., Bleck, W., 2018. Temperature dependent strain hardening and fracture behavior of TWIP steel. Int. J. Plast. 104, 80–103.

Maity, T., Prashanth, K.G., Balcı, Ö., Kim, J.T., Schöberl, T., Wang, Z., Eckert, J., 2018. Influence of severe straining and strain rate on the evolution of dislocation structures during micro-/nanoindentation in high entropy lamellar eutectics. Int. J. Plast. 109, 121–136.

Nutor, R.K., Cao, Q., Wei, R., Su, Q., Du, G., Wang, X., Li, F., Zhang, D., Jiang, J.Z., 2021. A dual-phase alloy with ultrahigh strength-ductility synergy over a wide temperature range. Sci. Adv. 7, eabi4404.

Pan, Q., Zhang, L., Feng, R., Lu, Q., An, K., Chuang, A.C., Poplawsky, J.D., Liaw, P.K., Lu, L., 2021. Gradient cell-structured high-entropy alloy with exceptional strength and ductility. Science 374, 984–989.

Peng, J., Li, L., Li, F., Liu, B., Zherebtsov, S., Fang, Q., Li, J., Stepanov, N., Liu, Y., Liu, F., Liaw, P.K., 2021. The predicted rate-dependent deformation behaviour and multistage strain hardening in a model heterostructured body-centered cubic high entropy alloy. Int. J. Plast. 145, 103073.

Qin, S., Yang, M., Jiang, P., Wang, J., Wu, X., Zhou, H., Yuan, F., 2022. Designing structures with combined gradients of grain size and precipitation in high entropy alloys for simultaneous improvement of strength and ductility. Acta Mater 230, 117847.

Ren, L., Xiao, W., Ma, C., Zheng, R., Zhou, L., 2018. Development of a high strength and high ductility near β-Ti alloy with twinning induced plasticity effect. Scr. Mater. 156, 47–50.

Senkov, O.N., Scott, J.M., Senkova, S.V., Miracle, D.B., Woodward, C.F., 2011a. Microstructure and room temperature properties of a high-entropy TaNbHfZrTi alloy. J. Alloys Compd. 509, 6043–6048.

Senkov, O.N., Wilks, G.B., Scott, J.M., Miracle, D.B., 2011b. Mechanical properties of $Nb_{25}Mo_{25}Ta_{25}W_{25}$ and $V_{20}Nb_{20}Mo_{20}Ta_{20}W_{20}$ refractory high entropy alloys. Intermetallics 19, 698–706.

Sheikh, S., Shafeie, S., Hu, Q., Ahlström, J., Persson, C., Veselý, J., Zýka, J., Klement, U., Guo, S., 2016. Alloy design for intrinsically ductile refractory high-entropy alloys. J. Appl. Phys. 120.

Shi, P., Li, R., Li, Y., Wen, Y., Zhong, Y., Ren, W., Shen, Z., Zheng, T., Peng, J., Liang, X., Hu, P., Min, N., Zhang, Y., Ren, Y., Liaw Peter, K., Raabe, D., Wang, Y.D., 2021. Hierarchical crack buffering triples ductility in eutectic herringbone high-entropy alloys. Science 373, 912–918.

Shi, P., Li, Y., Jiang, X., Shen, Z., Li, R., Lin, Z., Li, Q., Ding, B., Zheng, T., Liang, X., Min, N., Peng, J., Li, H., Ren, W., Lei, Z., Ren, Y., Liu, C.T., Zhong, Y., Ma, E., 2024. Strong-yet-ductile eutectic alloys employing cocoon-like nanometer-sized dislocation cells. Adv. Mater., 2405459 n/a.

Shuang, S., Hu, Y., Li, X., Yuan, F., Kang, G., Gao, H., Zhang, X., 2024. Tuning chemical short-range order for simultaneous strength and toughness enhancement in NiCoCr medium-entropy alloys. Int. J. Plast. 177, 103980.

Smith, L.T.W., Su, Y., Xu, S., Hunter, A., Beyerlein, I.J., 2020. The effect of local chemical ordering on Frank-Read source activation in a refractory multi-principal element alloy. Int. J. Plast. 134, 102850.

Tan, F., Li, J., Liu, B., Liaw, P.K., Fang, Q., 2024. Uncovering origin of grain boundary resistance to irradiation damage in NiCoCr multi-principal element alloys. Int. J. Plast. 175, 103925.

Ungár, T., Stoica, A.D., Tichy, G., Wang, X.L., 2014. Orientation-dependent evolution of the dislocation density in grain populations with different crystallographic orientations relative to the tensile axis in a polycrystalline aggregate of stainless steel. Acta Mater 66, 251–261.

Wang, F., Balbus, G.H., Xu, S., Su, Y., Shin, J., Rottmann, P.F., Knipling, K.E., Stinville, J.C., Mills, L.H., Senkov, O.N., Beyerlein, I.J., Pollock, T.M., Gianola, D.S., 2020. Multiplicity of dislocation pathways in a refractory multiprincipal element alloy. Science 370, 95–101.

Wang, L., Ding, J., Chen, S., Jin, K., Zhang, Q., Cui, J., Wang, B., Chen, B., Li, T., Ren, Y., Zheng, S., Ming, K., Lu, W., Hou, J., Sha, G., Liang, J., Wang, L., Xue, Y., Ma, E., 2023a. Tailoring planar slip to achieve pure metal-like ductility in body-centred-cubic multi-principal element alloys. Nat. Mater. 22, 950–957.

Wang, R., Tang, Y., Ai, Y., Li, S., Zhu, L.a., Bai, S., 2024. Strengthening and ductilization of a refractory high-entropy alloy over a wide strain rate range by multiple heterostructures. Int. J. Plast. 173, 103882.

Wang, S.P., Ma, E., Xu, J., 2019. New ternary equi-atomic refractory medium-entropy alloys with tensile ductility: hafnium versus titanium into NbTa-based solution. Intermetallics 107, 15–23.

Wang, W., Yuan, L., Zhang, H., Wei, Z., Zhang, H., Zhang, W., 2023b. Cold-rolled Ti-Al-V-Zr-Fe titanium alloy tubing with outstanding tensile properties. J. Alloys Compd. 931, 167558.

Wang, Z., Wu, H., Wu, Y., Huang, H., Zhu, X., Zhang, Y., Zhu, H., Yuan, X., Chen, Q., Wang, S., Liu, X., Wang, H., Jiang, S., Kim, M.J., Lu, Z., 2022. Solving oxygen embrittlement of refractory high-entropy alloy via grain boundary engineering. Mater. Today. 54, 83–89.

Wei, D., Gong, W., Tsuru, T., Lobzenko, I., Li, X., Harjo, S., Kawasaki, T., Do, H.S., Bae, J.W., Wagner, C., Laplanche, G., Koizumi, Y., Adachi, H., Aoyagi, K., Chiba, A., Lee, B.J., Kim, H.S., Kato, H., 2022. Si-addition contributes to overcoming the strength-ductility trade-off in high-entropy alloys. Int. J. Plast. 159, 103443.

Wen, X., Wu, Y., Huang, H., Jiang, S., Wang, H., Liu, X., Zhang, Y., Wang, X., Lu, Z., 2021. Effects of Nb on deformation-induced transformation and mechanical properties of $HfNb_xTa_{0.2}TiZr$ high entropy alloys. Mater. Sci. Eng. A 805, 140798.

Wu, Y.C., Shao, J.L., 2023. FCC-BCC phase transformation induced simultaneous enhancement of tensile strength and ductility at high strain rate in high-entropy alloy. Int. J. Plast. 169, 103730.

Xie, Z., Jian, W.R., Xu, S., Beyerlein, I.J., Zhang, X., Yao, X., Zhang, R., 2022. Phase transition in medium entropy alloy CoCrNi under quasi-isentropic compression. Int. J. Plast. 157, 103389.

Xu, Z.Q., Ma, Z.L., Tan, Y., Cheng, X.W., 2022. Designing TiVNbTaSi refractory high-entropy alloys with ambient tensile ductility. Scr. Mater. 206, 114230.

Yan, X., Zhang, Y., 2020. A body-centered cubic $Zr_{50}Ti_{35}Nb_{15}$ medium-entropy alloy with unique properties. Scr. Mater. 178, 329–333.

Yang, M., Pan, Y., Yuan, F., Zhu, Y., Wu, X., 2016. Back stress strengthening and strain hardening in gradient structure. Mater. Res. Lett. 4, 145–151.

Yeh, J.W., Chen, S.K., Lin, S.J., Gan, J.Y., Chin, T.S., Shun, T.T., Tsau, C.H., Chang, S.Y., 2004. Nanostructured high-entropy alloys with multiple principal elements: novel alloy design concepts and outcomes. Adv. Eng. Mater. 6, 299–303.

Yurchenko, N., Panina, E., Tojibaev, A., Novikov, V., Salishchev, G., Zherebtsov, S., Stepanov, N., 2023a. Effect of B2 ordering on the tensile mechanical properties of refractory $Al_xNb_{40}Ti_{40}V_{20-x}$ medium-entropy alloys. J. Alloys Compd. 937, 168465.

Yurchenko, N., Panina, E., Tojibaev, A., Novikov, V., Salishchev, G., Zherebtsov, S., Stepanov, N., 2023b. Tuning the grain and domain sizes to achieve superior room-temperature tensile ductility in a B2-ordered refractory $Al_{15}Nb_{40}Ti_{40}V_5$ medium-entropy alloy. Mater. Sci. Eng. A 874, 145073.

Zeng, S., Zhou, Y., Li, H., Zhang, H., Zhang, H., Zhu, Z., 2022. Microstructure and mechanical properties of lightweight $Ti_3Zr_{1.5}NbVAl_x$ ($x = 0$, 0.25, 0.5 and 0.75) refractory complex concentrated alloys. J. Mater. Sci. Technol. 130, 64–74.

Zhang, C., Wang, H., Wang, X., Tang, Y.T., Yu, Q., Zhu, C., Xu, M., Zhao, S., Kou, R., Wang, X., MacDonald, B.E., Reed, R.C., Vecchio, K.S., Cao, P., Rupert, T.J., Lavernia, E.J., 2023a. Strong and ductile refractory high-entropy alloys with super formability. Acta Mater 245, 118602.

Zhang, L.X., Liu, L., Guo, S., Pan, Q.S., Lu, L., 2024. Microstructure and evolution of gradient dislocation cells in multi-principal element alloy subjected to cyclic torsion. Acta Mater 275, 120059.

Zhang, S., Ding, X., Gao, X., Chen, R., Cao, W., Su, Y., Guo, J., 2023b. Dual enhancement in strength and ductility of Ti-V-Zr medium entropy alloy by fracture mode transformation via a heterogeneous structure. Int. J. Plast. 160, 103505.

Zhang, X., Wang, W., Wu, J., Wang, S., Sun, J., Chung, J.Y., Pennycook, S.J., 2021. Deformation twinning in $Ti_{48.9}Zr_{32.0}Nb_{12.6}Ta_{6.5}$ medium entropy alloy. Mater. Sci. Eng. A 809, 140931.

Zhu, Y., Ameyama, K., Anderson, P.M., Beyerlein, I.J., Gao, H., Kim, H.S., Lavernia, E., Mathaudhu, S., Mughrabi, H., Ritchie, R.O., Tsuji, N., Zhang, X., Wu, X., 2021. Heterostructured materials: superior properties from hetero-zone interaction. Mater. Res. Lett. 9, 1–31.

Zhu, Y., Wu, X., 2019. Perspective on hetero-deformation induced (HDI) hardening and back stress. Mater. Res. Lett. 7, 393–398.